

Exceptional points and symmetry recovery in a two-state system

Xu-Lin Zhang,^{1,2} Shubo Wang,¹ Wen-Jie Chen,¹ and C. T. Chan^{1,*}

¹*Department of Physics and Institute for Advanced Study, The Hong Kong University of Science and Technology, Clear Water Bay, Hong Kong, China*

²*State Key Laboratory on Integrated Optoelectronics, College of Electronic Science and Engineering, Jilin University, Changchun, China*

(Received 28 December 2016; published 7 August 2017)

We consider a two-state system consisting of a pair of coupled ferromagnetic waveguides. A monotonically increasing bias magnetic field can dynamically manipulate the system to enter a \mathcal{PT} -symmetry-broken phase and then reenter a symmetric phase. The symmetry recovery is enabled by the presence of accidental degeneracy points when the system has no loss and each degeneracy point can spawn a pair of exceptional points when asymmetric loss is introduced. We performed microwave experiments to demonstrate the presence of the exceptional point and symmetry recovery.

DOI: [10.1103/PhysRevA.96.022112](https://doi.org/10.1103/PhysRevA.96.022112)

I. INTRODUCTION

Non-Hermitian systems can possess real eigenvalues if their complex potential has parity-time (\mathcal{PT}) symmetry [1]. The system undergoes a transition at an exceptional point (EP) when the degree of non-Hermiticity is increased [2–4], after which the real parts of the eigenvalues coalesce while the imaginary parts bifurcate. In optics, \mathcal{PT} symmetry can be realized if the system possesses the symmetry $\varepsilon(x) = \varepsilon^*(-x)$ and $\mu(x) = \mu^*(-x)$ [5]. Although it is difficult to realize optical gain experimentally, EPs can also be found in passive non-Hermitian systems with asymmetric loss, which can be viewed as \mathcal{PT} -symmetric systems with a background of uniform loss [6]. The unique physics of EPs has given rise to many interesting phenomena and applications such as unusual beam dynamics [7,8], lasing effects [9–12], unidirectional transmissions [13,14], asymmetric mode switching [15], and others [16–23]. Exceptional points are typically manipulated by tuning gain and loss. When gain and loss are increased relative to coupling strength, there is only one EP for a two-state linear system and the \mathcal{PT} -symmetric state cannot be recovered once the system has entered the symmetry-broken phase. However, the system can reenter the \mathcal{PT} -symmetric phase if the system has more than two states [21,24,25] or if the system is nonlinear [26,27].

In this work we report the experimental observation of an EP and a subsequent symmetry recovery in a two-state system by tuning an external parameter adiabatically. We first investigate a \mathcal{PT} -symmetric coupled ferromagnetic waveguide system in the presence of a bias magnetic field. The system possesses multiple degeneracy points (DPs), which are diabolical points due to the absence of mode couplings at specific field strengths. Each DP becomes a pair of EPs when gain and loss are introduced. As a result, the system carries multiple EPs and exhibits symmetry-recovery behaviors in a dynamical process when the external field is tuned. Using a pair of waveguides, we experimentally demonstrate the presence of a pair of EPs originating from a single DP at microwave frequencies. Experimental measurements on the transmission spectra and field distributions clearly demonstrate the presence of the EP as well as symmetry recovery.

II. THEORETICAL DESIGN

We start by showing the physical mechanism underlying the presence of multiple EPs for a two-state system. Figure 1(a) illustrates the \mathcal{PT} -symmetric coupled ferromagnetic waveguide system with balanced gain and loss ($\varepsilon_1 = 12.3 - i\gamma$ and $\varepsilon_2 = 12.3 + i\gamma$). Static magnetic fields are applied to the two waveguides along opposite directions, inducing a diagonal term μ_b and off-diagonal terms $\pm i\chi$ of the permeability tensors [28]. The background material is assumed to have $\varepsilon_3 = 12$ and $\mu_3 = 1$. For the sake of simplicity, we first set $\mu_b = 1$, which does not affect the underlying physics. We calculate the dispersions of the weakly guided modes in this paraxial waveguide system without gain and loss ($\gamma = 0$) using COMSOL [29]. Figure 1(b) shows the effective mode index, defined as $n_{\text{eff}} = \beta_z/k_0$, with β_z and k_0 denoting the mode propagation constant and vacuum wave number, respectively, for the fourth pair of symmetric and antisymmetric modes as a function of χ (solid lines). Here χ depends on the external magnetic field, as will be stipulated later. For comparison, we show the dispersion of the fourth mode in a single waveguide (dashed line), which crosses the coupled symmetric-antisymmetric modes at two DPs. The mode degeneracy phenomenon has been reported in ferromagnetic waveguides in the presence of an external magnetic field due to the absence of mode couplings [30]. To substantiate this point, we define a mode-coupling coefficient $\eta = \iint (\mathbf{E}_1 \mathbf{D}_2^* + \mathbf{H}_1 \mathbf{B}_2^*) d\sigma$ to represent the coupling strength between the two waveguides, where the subscript j corresponds to the uncoupled eigenfield in the system with only waveguide j . Figure 1(c) shows the coupling coefficient between the uncoupled fourth set of modes. We find two regions with vanishing coupling strengths that match well with the two DPs in Fig. 1(b). The absence of mode couplings in this system can be attributed to the mode symmetry transition induced by the transverse bias magnetic fields from linear polarization to elliptical polarization (see Appendix A for a detailed discussion on the origin of the DPs as well as the behaviors of other order modes).

The coupled waveguide system without gain and loss can be described by a Hamiltonian of the form $H = \begin{bmatrix} \beta_0 & \kappa \\ \kappa^* & \beta_0 \end{bmatrix}$, where β_0 is the propagation constant of an uncoupled mode in the single waveguide and κ denotes the couplings between the two uncoupled modes. We use the numerical results in Fig. 1(b)

*Corresponding author: phchan@ust.hk

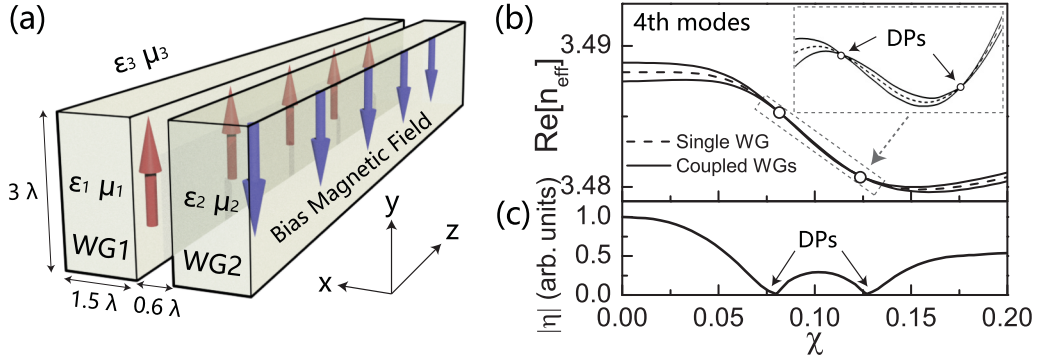


FIG. 1. (a) Schematic diagram of the coupled ferromagnetic waveguide system with bias magnetic fields applied along opposite directions. (b) Calculated effective mode index of the fourth pair of modes in the coupled system (solid lines) and that of the fourth mode in a single waveguide (dashed line) as a function of χ with $\gamma = 0$, where we find two degeneracy points. (c) Calculated mode-coupling coefficient $|\eta|$ (see the text for definition).

to fit κ as a function of χ . Figure 2(a) plots the fitted curve (solid line), showing that κ displays a similar dependence on χ as the coupling coefficient η in Fig. 1(c). In fact, κ and η are calculated based on the eigenvalues and eigenfields, respectively, and they both support the finding of DPs in the proposed system. We then introduce gain and loss into the system. We show three cases of gain and loss ($\gamma = 3 \times 10^{-4}$, 4.9×10^{-4} , and 2×10^{-3}) in Figs. 2(b)–2(d), respectively, where the effective mode index becomes complex. A \mathcal{PT} -broken phase emerges at an EP when the gain or loss parameter becomes larger than the coupling. As the coupling is vanishing at the DPs, we expect that even a very small γ can give rise to EPs. This is indeed the case, as shown in Fig. 2(b), where a small $\gamma = 3 \times 10^{-4}$ is sufficient to turn each DP into a pair

of EPs. For ordinary two-level systems, there is only one EP and the \mathcal{PT} -symmetry of eigenmodes remains broken beyond the EP. However, as χ increases, our system first enters a \mathcal{PT} -broken phase but reenters a \mathcal{PT} -symmetric phase before becoming \mathcal{PT} -broken again. \mathcal{PT} -symmetry recovery has been reported in multistate systems [21,24,25], but it occurs here in a two-state system. When the gain or loss reaches a particular threshold ($\gamma = 4.9 \times 10^{-4}$), the right-hand EP of the left bubble and the left-hand EP of the right bubble merge to form one EP, as shown in Fig. 2(c). Increasing γ further, the two \mathcal{PT} -broken phase regions merge into one so that the broken-symmetry regime broadens [Fig. 2(d)]. To better understand the variation of the eigenmode behaviors, we plot the calculated magnitude of the imaginary part of the propagation constant (defined

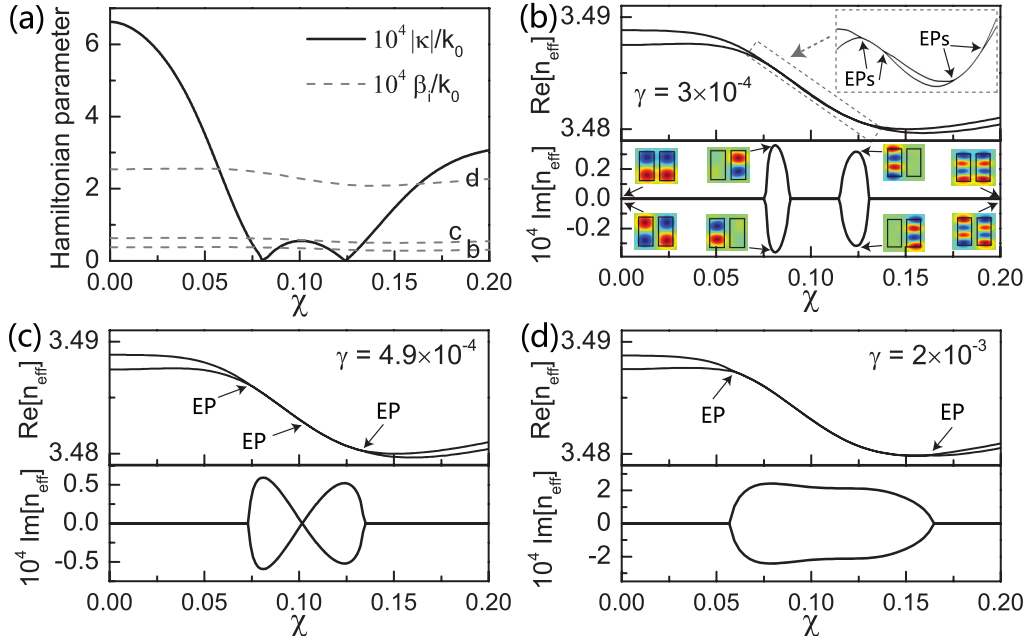


FIG. 2. (a) Coupling parameter κ (solid line) obtained through fitting for the fourth pair of modes in the system without gain and loss. The dashed lines show the calculated imaginary part of the effective mode index of the fourth mode in a single waveguide with gain and loss corresponding to those in (b)–(d). (b)–(d) Calculated effective mode index of the fourth pair of modes with different gain and loss: (b) $\gamma = 3 \times 10^{-4}$, (c) $\gamma = 4.9 \times 10^{-4}$, and (d) $\gamma = 2 \times 10^{-3}$. We find multiple EPs and symmetry recovery behaviors. The inset of (b) shows H_y eigenfield distributions at different χ , showing features typical of \mathcal{PT} -symmetric and \mathcal{PT} -broken regions.

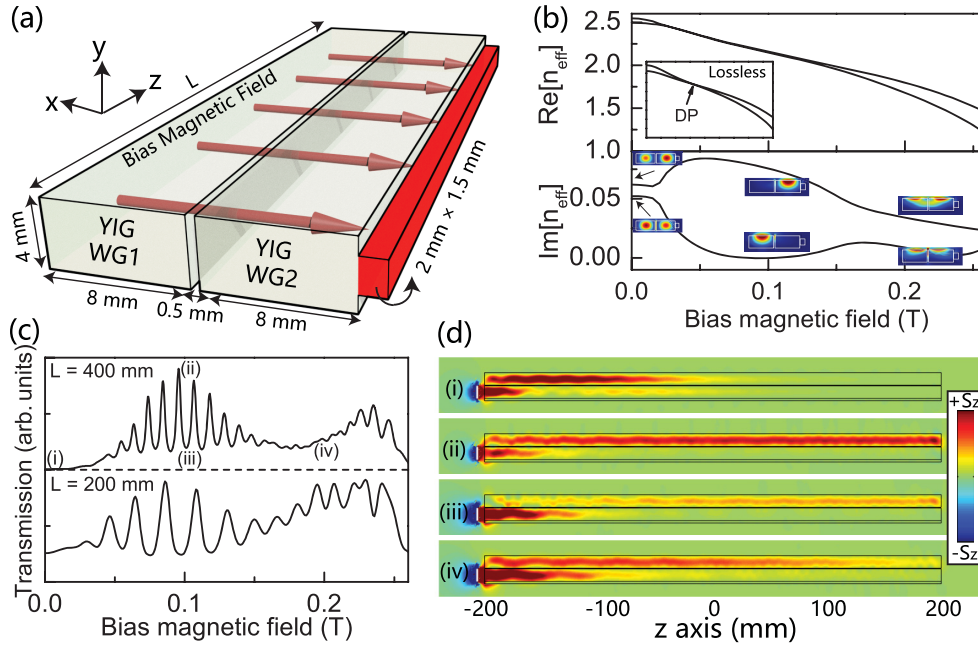


FIG. 3. (a) Schematic diagram of a passive coupled YIG waveguide system with microwave absorbers attached to the side of one waveguide. (b) Calculated effective mode index as a function of the bias magnetic field, in which we find the salient feature of an EP as well as symmetry recovery. The inset of the upper panel shows the results for the lossless coupled system, where a DP appears and can spawn a pair of EPs when an absorber is added. The inset of the lower panel (see the six colored patterns) shows the power flow distributions on the x - y plane at different bias magnetic fields. (c) Numerically simulated transmission spectra as a function of the magnetic field for $L = 200$ and 400 mm, where a region with enhanced transmission can be found that matches well with the broken phase region predicted in (b). The peaks correspond to Fabry-Pérot resonances. (d) Power flow distributions in the coupled system with $L = 400$ mm for different magnetic fields marked as (i)–(iv) in (c). The field patterns in (iii) and (iv) have been scaled up by a factor of 2 for improved readability. The frequency is 9.5 GHz in all of these simulations.

as $\beta_r \pm i\beta_i$) in a single waveguide for the above three cases of gain and loss in Fig. 2(a) (see the dashed lines). We see that the regimes corresponding to $|\kappa| < \beta_i$ match well with the numerically obtained \mathcal{PT} -broken phase regimes in Figs. 2(b)–2(d).

In fact, a system with asymmetric losses (rather than exact \mathcal{PT} symmetry) already exhibits the aforementioned effects. We design a non-Hermitian passive system consisting of a pair of yttrium iron garnet (YIG) dielectric waveguides placed in air working at microwave frequencies. Microwave absorbers are attached to the side of YIG waveguide 2 [red region in Fig. 3(a)] to introduce asymmetric losses into the system, given that the intrinsic dielectric loss of YIG is negligible. We apply a bias magnetic field along the $-x$ axis. The eigenfield distributions move towards the $+y$ interface due to the field displacement effect when the transverse bias magnetic field is perpendicular to the rf magnetic field [28]. Exceptional points and symmetry recovery can also appear in this configuration due to the field-induced variation of mode couplings. We first theoretically analyze the eigenmodes supported in this system. The permeability tensor of YIG is modeled with $\mu_b = 1 + \omega_m \omega_0 / (\omega_0^2 - \omega^2)$ and $\chi = \omega_m \omega / (\omega_0^2 - \omega^2)$, where $\omega_0 = \mu_0 \gamma_R H_0$ is determined by the gyromagnetic ratio γ_R and bias magnetic field H_0 and $\omega_m = \mu_0 \gamma_R M$ is determined by the magnetization M , which is measured experimentally as shown in Fig. 4(a). Here permeability losses can be ignored because the system works far away from the gyromagnetic resonance. Figure 3(b) shows the calculated effective mode

index of the coupled YIG waveguides at 9.5 GHz as a function of the bias magnetic field. In the simulation, the permittivity of YIG and the microwave absorber are chosen as ~ 15.2 [31] and $\sim 4 + 15i$ [see Fig. 4(b)], respectively. Given the structure parameters [see Fig. 3(a)] and frequency (~ 9.5 GHz), the coupled system supports only two eigenmodes, indicating that each waveguide is in fact operating at the single-mode condition. We find a region (0.02–0.16 T) where the real parts of the two modes almost coalesce while the corresponding imaginary parts first repel and then attract each other again. This is a typical feature of an EP associated with the symmetry recovery. The inset of Fig. 3(b) shows the presence of a DP when the microwave absorber is removed. This DP spawns a pair of EPs when asymmetric losses are introduced and symmetry recovery naturally arises. The power flow distributions of the eigenmodes are also shown in the inset

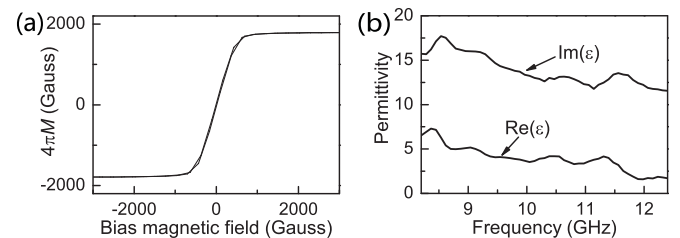


FIG. 4. (a) Measured hysteresis loop of YIG. (b) Measured permittivity of the microwave absorber.

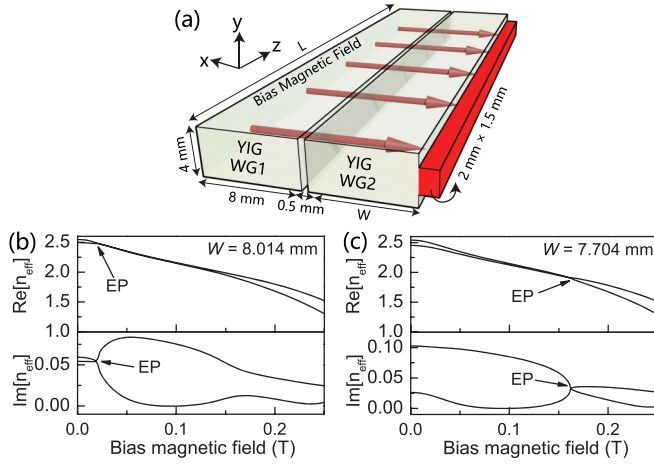


FIG. 5. (a) Schematic diagram of a YIG coupled waveguide system in which the width of waveguide 2 is denoted by W . (b) Calculated effective mode index at 9.5 GHz as a function of the bias magnetic field with $W = 8.014$ mm, where the EP can be accessed at 0.019 T. (c) Items shown are the same as in (b) but with $W = 7.704$ mm, where the symmetry recovery point can be accessed at 0.162 T.

of Fig. 3(b), where the field displacement effect can be found. The symmetry of the eigenmode (PT symmetric or broken) is also evident.

In Fig. 3(b) we note that the real and imaginary parts are separated in the broken and/or symmetric phase region. This is due to the mode detuning induced by the broken symmetry of the two waveguides, i.e., only one waveguide is attached with the microwave absorber. In other words, the system is very close to the “exact” EP and symmetry recovery point. We show that the EPs can be accessed if we slightly tune a parameter of the system such as the width of YIG waveguide 2. The studied system is shown in Fig. 5(a), where W denotes the width of YIG waveguide 2 and the other parameters are the same as those in Fig. 3(a). It turns out that the EP and symmetry-recovery point can be accessed with $W = 8.014$ and 7.704 mm, as shown in Fig. 5(b) and 5(c), respectively. Although the EPs can never be accessed in experiments, creating a system that is very close to the EPs as we show in this work is sufficient to study the physics and consequences of EPs.

III. EXPERIMENTAL REALIZATIONS

We performed microwave experiments to implement the theoretical design. A photograph of the experimental setup is shown in Fig. 6(a), where a pair of YIG waveguides

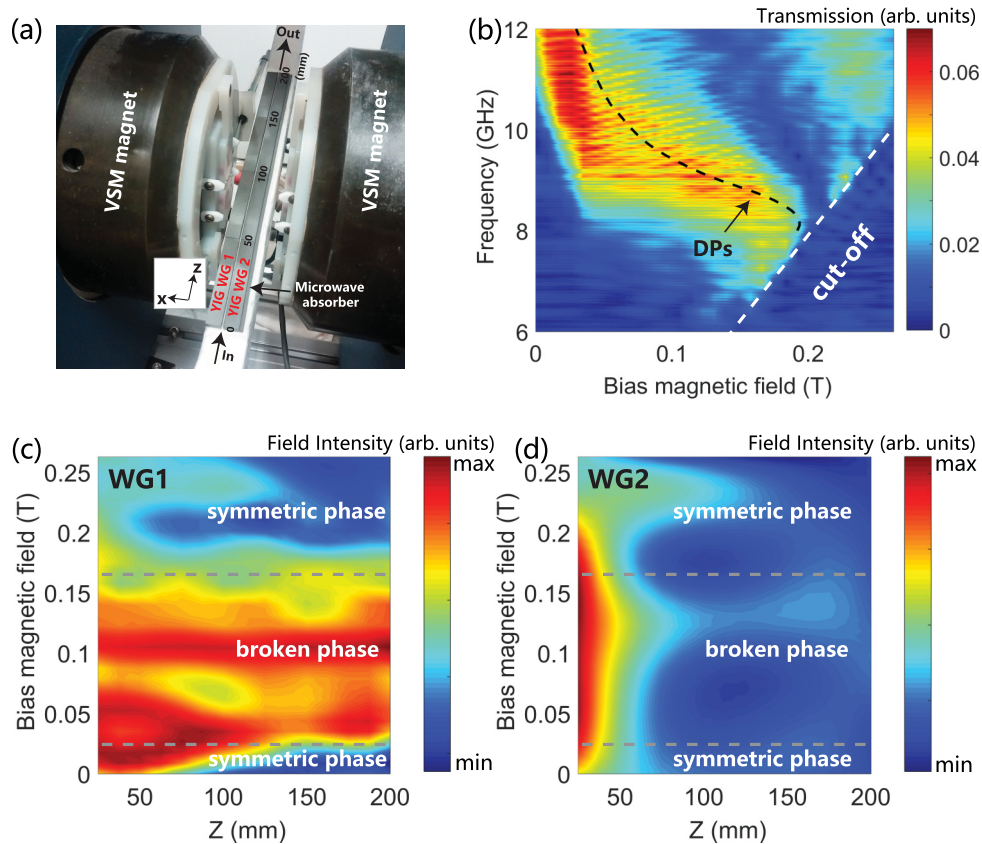


FIG. 6. (a) Photograph of the coupled YIG waveguide system placed inside a vibrating sample magnetometer. Microwave absorbers are attached on the side of one waveguide. Each waveguide measures $8 \times 4 \times 200$ mm³ and the gap distance is 0.5 mm. (b) Experimentally measured transmission spectra for different magnetic-field strengths and frequencies, where the black dashed line shows the calculated DPs. The modes are cut off in the region below the white dashed line. (c) and (d) Experimentally measured surface electric-field intensity along the propagation direction [see (a) for the definition of z axis] at 9.5 GHz for (c) waveguide 1 and (d) waveguide 2. The two gray dashed lines mark the boundary between symmetric phase and broken phase regimes.

($8 \times 4 \times 200 \text{ mm}^3$) with a gap of $\sim 0.5 \text{ mm}$ are placed inside a vibrating sample magnetometer, which can provide a quasiuniform bias magnetic field along the $-x$ axis in the area of interest (see Appendix B for a discussion of the uniformity of the bias field). The transmission spectra of the system were measured to identify the EP as well as the symmetry-recovery behavior, since the transmission is enhanced in the broken phase region [6]. We placed an antenna near the surface of the lossy waveguide, which breaks the symmetry so that the two eigenmodes in the system can both be excited sufficiently. Another antenna was used on the other side of the system to receive the transmission power. Both antennas were connected to the cable of an Agilent Technologies 8720ES Network Analyzer for measuring the transmission spectra. The measured transmission spectra for different magnetic-field strengths and frequencies are plotted in Fig. 6(b). We observe that for each frequency there is a considerable transmission enhancement at some specific bias fields. The enhanced transmission regime corresponds to the symmetry-broken phase, in which the wave can travel a longer distance in the waveguide without the absorber. For example, we observe enhanced transmission at 9.5 GHz mainly between 0.02 and 0.16 T, which matches well with the broken phase region predicted in Fig. 3(b). This enhanced region shifts to higher external fields at lower frequencies, which is due to the shift of the DPs in the lossless system. The black dashed line in Fig. 6(b) marks the calculated DPs, which lies almost at the center of the experimental broken phase region, indicating that the EPs are indeed spawned from the DPs.

To investigate the underlying physics, we measured the electric-field intensity on the surface of each waveguide along the waveguiding direction [see the z axis in Fig. 6(a)]. The experimental results at 9.5 GHz for different bias fields are shown in Figs. 6(c) and 6(d), respectively, for waveguide 1 and waveguide 2. The transmission enhancement regime at 9.5 GHz estimated from Fig. 6(b) is marked by the two gray dashed lines, which divide the regime into two symmetric phases and one broken phase. In the symmetric phase regime, both the symmetric and antisymmetric modes experience considerable losses, meaning that the electric-field intensity decays exponentially along the direction of propagation in both waveguide 1 [Fig. 6(c)] and waveguide 2 [Fig. 6(d)]. In the broken phase region, however, the two eigenmodes propagate individually in the two waveguides [see the power flow patterns in the inset of Fig. 3(b)]. As a result, the wave in waveguide 1 can travel a longer distance since the mode losses are small [Fig. 6(c)], while the wave in waveguide 2 experiences high losses because of the attached absorber [Fig. 6(d)]. The transmission of the whole system is then increased as a result of the longer transport distance in the lossless waveguide 1. The high contrast of the field distributions in the two waveguides strongly demonstrates the presence of the symmetric phase and broken phase.

We show numerical simulation results to support the above experimental results. To calculate the transmission spectra, we place a line current source [white lines in Fig. 3(d)] near the edge of the lossy waveguide to mimic the antenna in experiments. The power flow S_z at the output surface is integrated to provide the transmission. The calculated transmission spectrum of the system at 9.5 GHz with a length

of 200 mm, which can reproduce the salient features observed in experiments, is shown in Fig. 3(c). The transmission exhibits an oscillating behavior in both experiments and simulations due to the Fabry-Pérot resonance associated with the change in effective mode index under the variation of the bias magnetic field for a waveguide of a finite length. A further increase in the waveguide length to 400 mm in the simulation can double the resonant peak number [see Fig. 3(c)], confirming the presence of the Fabry-Pérot effect. We show in Fig. 3(d) the calculated power flow distributions for four cases marked (i)–(iv) in Fig. 3(c) to show the mode behaviors in the symmetric phase regime [(i) and (iv)] and broken phase regime [(ii) and (iii)]. The simulated field distributions coincide with the experimental results in Figs. 6(c) and 6(d). We also note from Fig. 3(c) that after the broken phase region, the transmission again increases when the field is greater than 0.2 T [also see Fig. 6(b) for experiment]. This is due to the overall decrease in mode losses [see the imaginary part in Fig. 3(b)] as field strength increases because a stronger external field can displace the eigenfield from the absorber [see the field patterns in Fig. 3(b)]. A further increase in the external field drives the two eigenmodes close to the cutoff [see the real part in Fig. 3(b); also refer to the white dashed line in Fig. 6(b)] as μ_b approaches zero [28]. As a result, the transmission shows a sudden drop. All these numerical results are consistent with the above experimental results, demonstrating the presence of EPs as well as symmetry-recovery behaviors.

IV. CONTROL EXPERIMENTAL RESULTS

We show four sets of control experimental results in this section to further support the findings in this work.

A. Control experiment I: Rotating the system by 90°

We performed a control experiment in which the coupled waveguide system is rotated by 90° taking the z axis as the shaft. In this case the bias field is parallel to the short edge of the YIG waveguide, as shown in Fig. 7(a). The calculated effective mode index as a function of the bias magnetic field at 9.5 GHz is shown in Fig. 7(b). We find that in the field range of interest, there is no EP-related phenomenon. This is due to the fact that the system does not possess a DP when the microwave absorber is absent [see the inset of Fig. 7(b)]. The measured transmission spectra at different bias magnetic fields are shown in Fig. 7(c). These spectra look almost the same, indicating that such a configuration really does not support the presence of EPs. This control experiment can further support our conclusion that the enhanced transmission in Fig. 6(b) is due to the presence of EPs and symmetry recovery.

B. Control experiment II: Increasing the gap distance

We performed another control experiment in which the gap distance between the two YIG waveguides is increased to $g = 2 \text{ mm}$. The measured transmission spectra are shown in Fig. 8(c), where we find that the broken phase region becomes broader than that of the case $g = 0.5 \text{ mm}$ [see Fig. 6(b)]. To explain this phenomenon, we calculate the effective mode index of the lossless system at 9.5 GHz and show the results

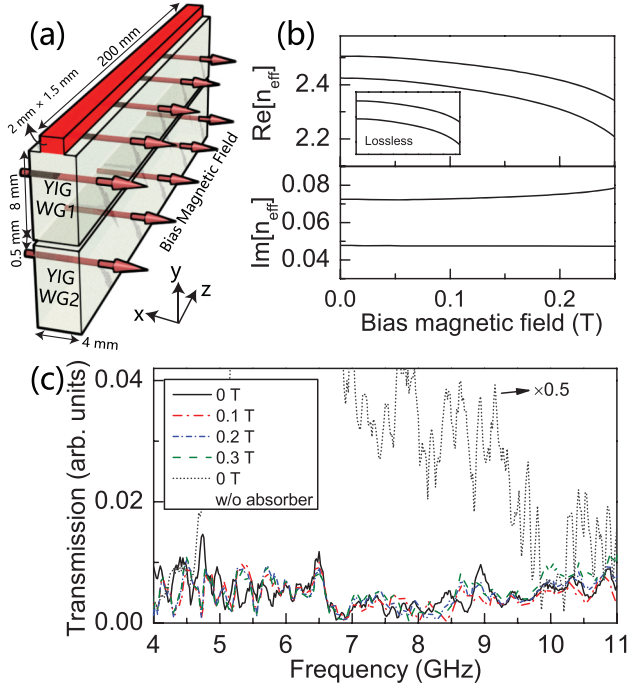


FIG. 7. (a) Schematic diagram of a coupled ferromagnetic waveguide system with the bias magnetic field parallel to the short edge of the waveguide. (b) Calculated effective mode index as a function of the bias magnetic field at 9.5 GHz. The inset shows the effective mode index in the lossless system, showing the absence of DPs. (c) Measured transmission spectra with different bias-field strengths, where the gray dashed line shows the result for the system without the absorber attached.

in Fig. 8(a). We note that the position of the DP exhibits a shift compared to the case of $g = 0.5$ mm. In other words, the DP will appear at a lower bias field when the gap distance is increased. This trend is also shown in Fig. 8(d) for different frequencies (comparing the red line and black line). The shift of the DP in the lossless system results in a corresponding shift of the broken phase region in the lossy system. We plot in Fig. 8(b) the calculated imaginary part of the effective mode index of the lossy system. It turns out that with a larger gap distance of 2 mm, the system with a zero-bias field at 9.5 GHz is already in the broken phase region [also see Fig. 8(c)]. The mode coupling becomes weaker when the gap distance is increased. As a consequence, with the same microwave absorber attached, the bandwidth of the broken phase region becomes broader [see Fig. 8(b) for theoretical results, Fig. 8(c) for experimental phenomena, and Fig. 2(a) for interpretation].

C. Control experiment III: Removing the microwave absorber

We performed a third control experiment in which the microwave absorber is removed, as illustrated schematically in Fig. 9(a). Figure 9(b) shows the measured transmission spectra of this system with different bias magnetic fields and the results for three typical frequencies are given in Fig. 9(c). By investigating the spectra, we do not observe the aforementioned enhanced transmissions, indicating that the observed transmission enhancement in Fig. 6(b) is not due to some coupling effects between two lossless waveguides but deeply related to the microwave absorber since EPs can only exist in non-Hermitian systems.

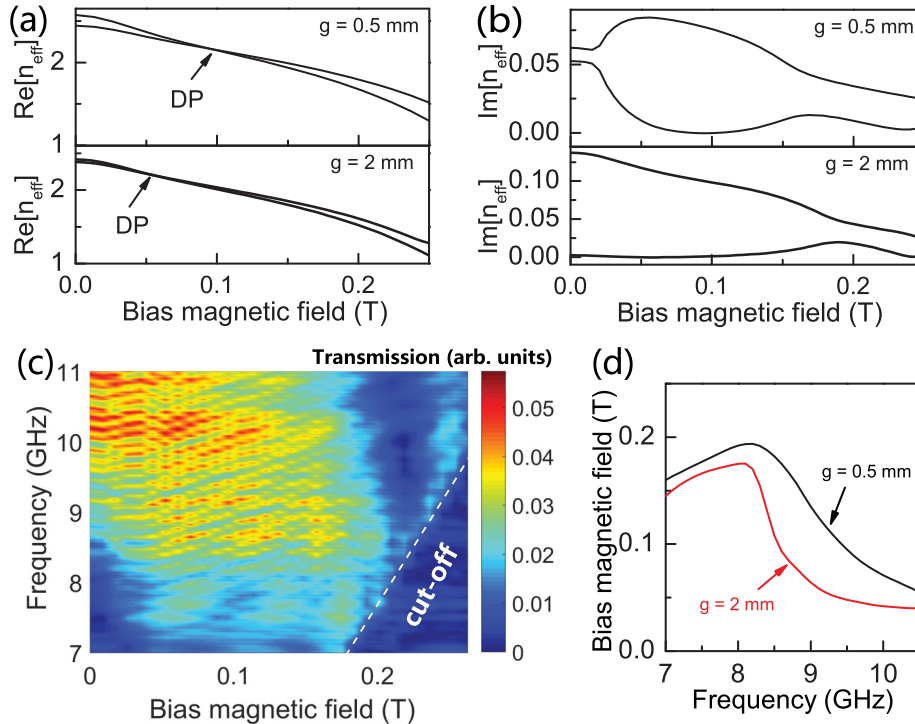


FIG. 8. Calculated effective mode index as a function of the bias magnetic field in the (a) lossless system and (b) lossy system with different gap distances at 9.5 GHz. (c) Measured transmission spectra of the system with $g = 2$ mm as a function of bias fields and frequencies. (d) Calculated bias magnetic field required to reach the DP in the lossless system with $g = 0.5$ and 2 mm.

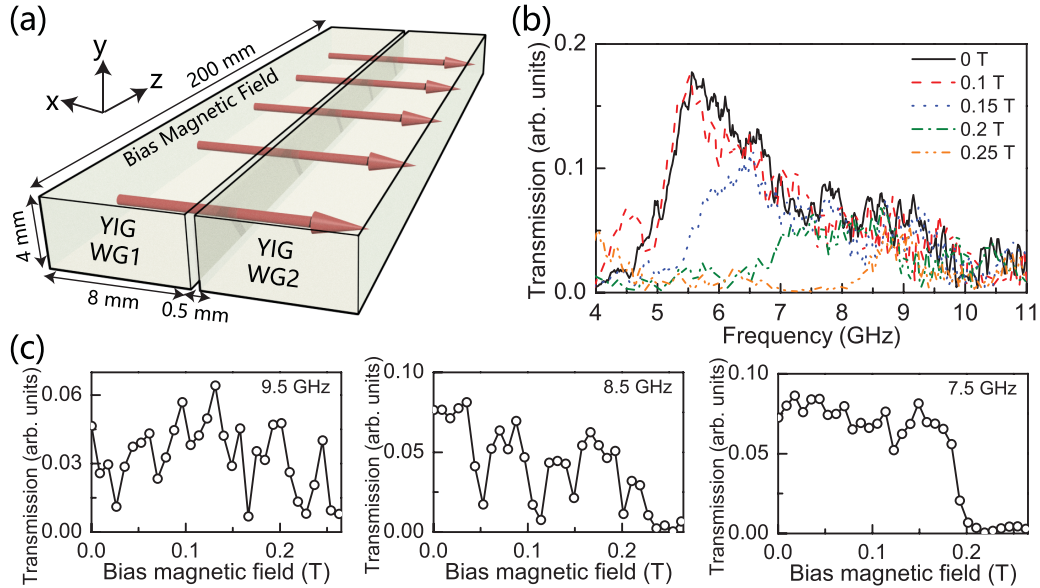


FIG. 9. (a) Schematic diagram of the coupled system without the microwave absorber attached. (b) Measured transmission spectra of this system with different bias-field strengths. (c) Measured transmission intensities as a function of the bias field for three typical frequencies.

D. Control experiment IV: Single YIG waveguide with the microwave absorber

We performed a fourth control experiment by studying a single YIG waveguide with the microwave absorber attached [see Fig. 10(a)]. Figure 10(b) shows the measured transmission spectra of this system with different bias magnetic fields. It turns out that these spectra are almost the same, demonstrating that the observed transmission enhancement in Fig. 6(b) is not due to the variation of mode losses as the bias field increases. To create an EP, at least two modes are required in non-Hermitian systems.

V. SUMMARY

To conclude, we have shown both theoretically and experimentally that in a two-state coupled ferromagnetic waveguide system, EPs can be manipulated by tuning a bias magnetic field, creating multiple EPs and symmetry-recovery behaviors that are rarely seen in two-state systems. Compared to conventional EP systems based on tuning gain and loss, the tuning process in this work is both adiabatic and continuous. This process can be employed to tune system parameters to

encircle an EP to manifest the topological properties of the system [15,32,33] and may be applicable to the nonreciprocal transport of electromagnetic waves and communications.

ACKNOWLEDGMENTS

This work was supported by the Hong Kong Research Grants Council through Grant No. AoE/P-02/12. X.-L.Z. was also supported by the National Natural Science Foundation of China (Grant No. 61605056) and the China Postdoctoral Science Foundation (Grant No. 2016M591480).

APPENDIX A: ORIGIN OF THE DEGENERACY POINTS

1. Mode analysis

We give a detailed study on the origin of the DPs. We first consider the coupled ferromagnetic waveguide system shown in Fig. 1(a). Under the bias magnetic fields, the permeability tensors take the form

$$\mu_1 = \begin{bmatrix} \mu_b & 0 & i\chi \\ 0 & 1 & 0 \\ -i\chi & 0 & \mu_b \end{bmatrix}, \quad \mu_2 = \begin{bmatrix} \mu_b & 0 & -i\chi \\ 0 & 1 & 0 \\ i\chi & 0 & \mu_b \end{bmatrix}. \quad (\text{A1})$$

Figure 11(a) shows the calculated effective mode index of the first four pairs of modes as a function of χ . Each pair of modes consists of a symmetric and an antisymmetric mode as a result of waveguide couplings. We find that multiple DPs can be supported in the system (see the circles) due to the absence of mode couplings at specific values of χ . To further explore the origin of the absence of mode couplings, we study a single ferromagnetic waveguide under a bias magnetic field [see the inset of Fig. 11(b)] and show the corresponding effective mode index as a function of χ in Fig. 11(b). The variation of the eigenfield characteristics of the single waveguide mode under a bias magnetic field should account for the origin of DPs. To show this point, we illustrate

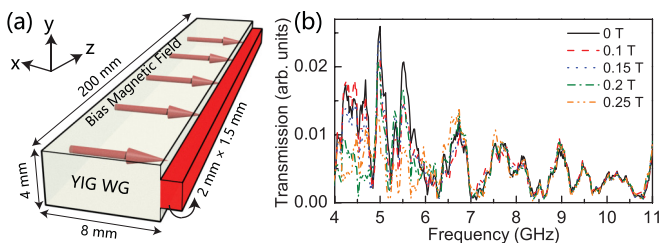


FIG. 10. (a) Schematic diagram of a single YIG waveguide with the microwave absorber attached. (b) Measured transmission spectra of this system with different bias-field strengths.

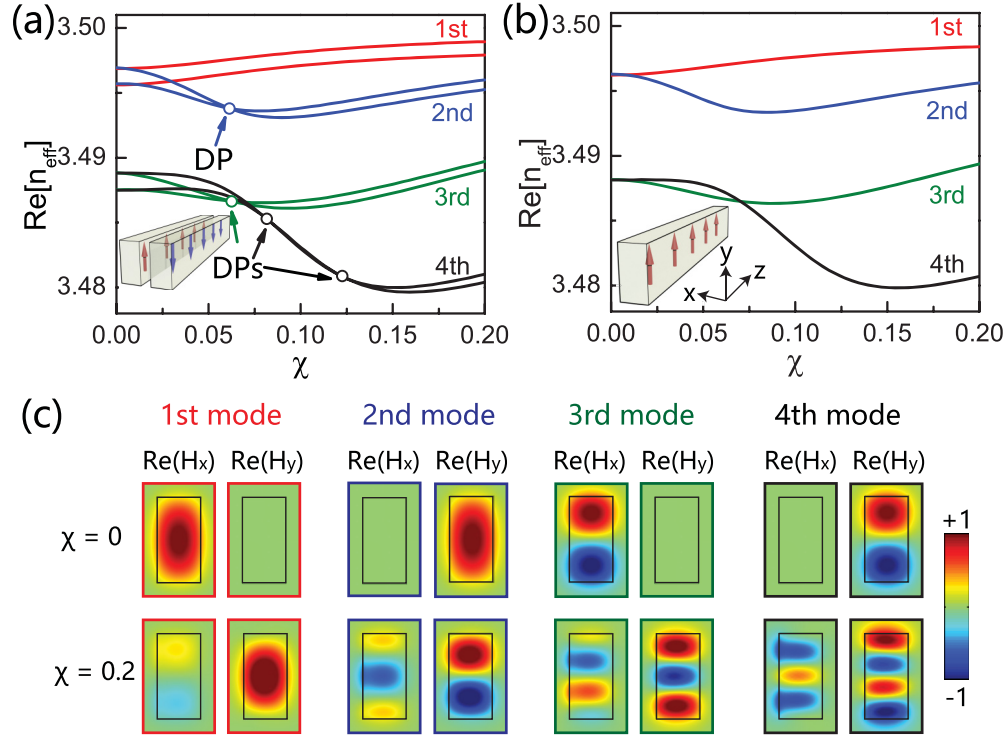


FIG. 11. (a) Calculated effective mode index of the first four pairs of modes in the coupled waveguides as a function of χ . (b) Calculated effective mode index of the first four modes in the single waveguide as a function of χ . (c) Magnetic-field distributions for the first four modes in the single waveguide with $\chi = 0$ and 0.2.

in Fig. 11(c) the magnetic-field distributions H_x and H_y in the single waveguide for the first four modes with $\chi = 0$ (upper figures) and $\chi = 0.2$ (lower figures). When the bias field is absent ($\chi = 0$), the eigenmodes are linearly polarized and the first, second, third, and fourth modes are E_y/H_x , E_x/H_y , E_y/H_x , and E_x/H_y polarized, respectively. The polarization of the eigenmodes becomes elliptical as evidenced by the coexistence of x - and y -field components when a transverse bias field is applied as shown by the results with $\chi = 0.2$. Then we see a significant change of the eigenmode characteristics, i.e., from linear polarization to elliptical polarization upon increasing the bias magnetic field. Since the bias magnetic field in the two waveguides is along opposite direction, in the above transition process the corresponding eigenfields should change in a different way, which results in the absence of mode couplings associated with DPs. The absence of mode

couplings at a specific value of $\chi = 0.0816$ can be understood from Fig. 12, where we show the field distributions of the two uncoupled fourth set of modes, corresponding to the first DP of the fourth pair of modes in Fig. 11(a). An integration of the two uncoupled eigenfields via $\eta = \iint (\mathbf{E}_1 \mathbf{D}_2^* + \mathbf{H}_1 \mathbf{B}_2^*) d\sigma$ gives a zero coupling strength. The z component of the eigenfield is very small and therefore is not shown here.

We can follow the same way to demonstrate the presence of a DP in the coupled YIG waveguide system shown in Fig. 3(a). We calculate the coupling strength and show the result in Fig. 13(a). The vanishing coupling strength at ~ 0.095 T can account for the DP in the inset of Fig. 3(b). We further show in Fig. 13(b) the eigenfield patterns of the two uncoupled modes in a single YIG waveguide at this DP. The integration between the two eigenfields via $\eta = \iint (\mathbf{E}_1 \mathbf{D}_2^* + \mathbf{H}_1 \mathbf{B}_2^*) d\sigma$ is exactly zero at this point.

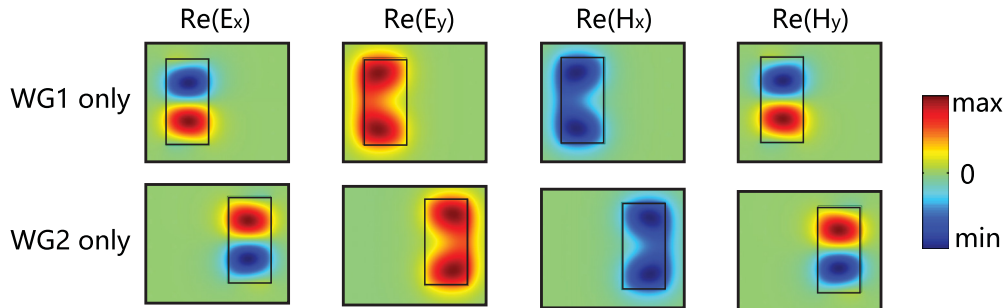


FIG. 12. Eigenfield patterns of the two uncoupled fourth set of modes in a single waveguide with $\chi = 0.0816$. At the same value, a DP appears between the fourth pair of modes in the coupled waveguides. The integration of the field patterns gives a zero coupling strength.

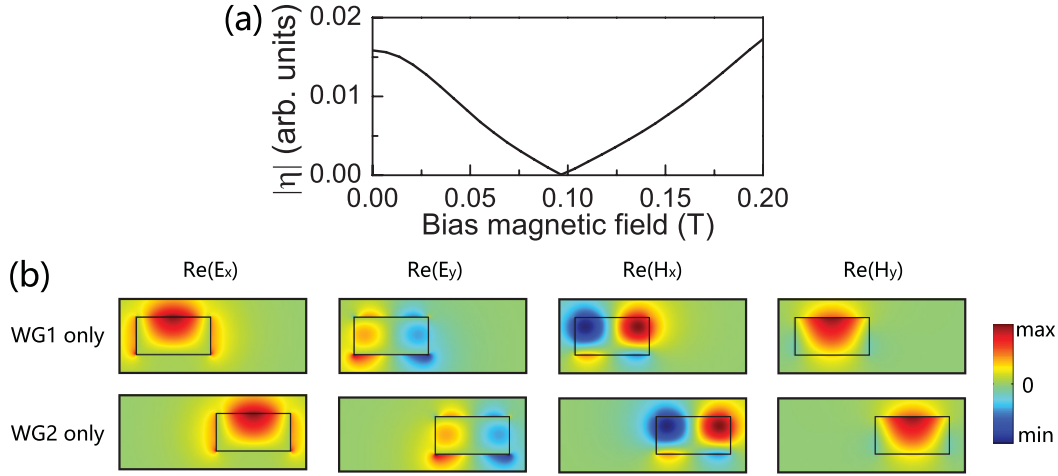


FIG. 13. (a) Coupling coefficient between the two uncoupled fundamental modes in the coupled system shown in Fig. 3(a). The frequency is 9.5 GHz. (b) Eigenfield patterns of the two uncoupled modes in a single YIG waveguide with a bias magnetic field of ~ 0.095 T, corresponding to the case of the DP in (a).

2. Slab model

We apply a simple slab model to investigate the mode behavior when a bias magnetic field is applied. Consider a ferromagnetic slab (ϵ_r, μ_r) with air on either side of the slab boundary. The two boundaries are parallel to the z - x plane and

the guided mode is propagating along the z axis. We apply a bias magnetic field along the y axis. Assuming $\partial/\partial z = i\beta$ and applying $\partial/\partial x = 0$, where β is the mode propagation constant, the Maxwell equations read

$$\left\{ \begin{array}{l} i\beta E_x = i\omega\mu_0 H_y \\ \frac{\partial E_x}{\partial y} = -\omega\mu_0\chi H_x - i\omega\mu_0\mu_b H_z \\ i\beta H_y - \frac{\partial H_z}{\partial y} = i\omega\epsilon_0\epsilon_r E_x \end{array} \right. \quad \left\{ \begin{array}{l} i\beta H_x = -i\omega\epsilon_0\epsilon_r E_y \\ \frac{\partial H_x}{\partial y} = i\omega\epsilon_0\epsilon_r E_z \\ i\beta E_y - \frac{\partial E_z}{\partial y} = -i\omega\mu_0\mu_b H_x + \omega\mu_0\chi H_z \end{array} \right. \quad (\text{A2})$$

We find that when the bias field is absent ($\mu_b = 1$ and $\chi = 0$), there are two types of solutions, i.e., the TE modes (E_x , H_y , and H_z) and TM modes (H_x , E_y , and E_z). In the presence of the bias field ($\chi \neq 0$), the TE modes and TM modes are coupled via χ so that the eigenmodes acquire all the field components (E_x , E_y , E_z , H_x , H_y , and H_z). That is the reason why we find in Fig. 11 that all the field components emerge at $\chi = 0.2$.

After some derivations of Eq. (A2), we have the equation for E_x :

$$\begin{aligned} \frac{\partial^4 E_x}{\partial y^4} + [2\omega^2\mu_0\mu_b\epsilon_0\epsilon_r - (1 + \mu_b)\beta^2] \frac{\partial^2 E_x}{\partial y^2} \\ + \left(\omega^2\mu_0\mu_b\epsilon_0\epsilon_r - \beta^2 - \omega^2\mu_0\epsilon_0\epsilon_r \frac{\chi^2}{\mu_b} \right) \\ \times (\omega^2\mu_0\mu_b\epsilon_0\epsilon_r - \mu_b\beta^2) E_x = 0. \end{aligned} \quad (\text{A3})$$

We simply set $\mu_b = 1$ and define $\zeta = \omega^2\mu_0\epsilon_0\epsilon_r - \beta^2$ and $\xi = \omega^2\mu_0\epsilon_0\epsilon_r\chi^2$. Then Eq. (A3) becomes $\frac{\partial^4 E_x}{\partial y^4} + 2\zeta \frac{\partial^2 E_x}{\partial y^2} + \zeta(\zeta - \xi)E_x = 0$. The y dependence of E_x should take the form

$$\begin{aligned} E_x = A \exp(i\alpha_1 y) + B \exp(i\alpha_2 y) + C \exp(-i\alpha_1 y) \\ + D \exp(-i\alpha_2 y), \end{aligned} \quad (\text{A4})$$

where we have defined $\alpha_{1,2} = \sqrt{\zeta \pm \sqrt{\zeta^2 - \xi}}$ and A , B , C , and D are coefficients to be determined. There are two \mathbf{k} , i.e., α_1 and α_2 , coexisting in the ferromagnetic layer due to the nonreciprocity induced by the bias magnetic field, whereas in a reciprocal system the two \mathbf{k} should be degenerate. The difference between α_1 and α_2 depends on χ and their interference determines the eigenfields in the waveguide. We then find in Fig. 11 that there are more standing waves along the y direction when the bias field is applied.

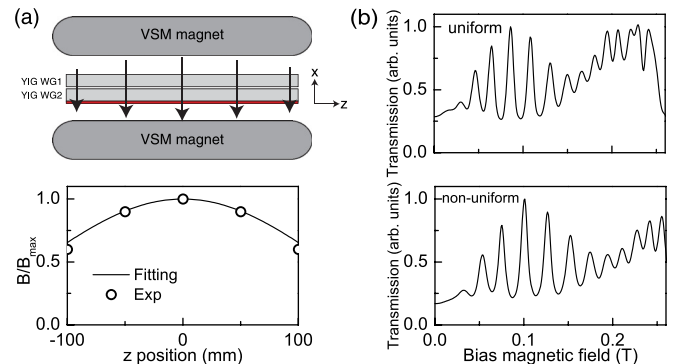


FIG. 14. (a) Nonuniformity of the bias magnetic field acting on the system. (b) Calculated transmission spectra with uniform and nonuniform bias fields.

APPENDIX B: NONUNIFORMITY OF THE BIAS FIELDS

The external magnetic field acting on the coupled waveguide system with a length of 200 mm is actually not uniform, but we show in this appendix that this slight nonuniformity will not affect the phenomena expected in experiments. Figure 14(a) shows the measured bias magnetic fields at

different positions (circles), which are fitted with the solid line for numerical simulations. We then calculate the transmission spectrum at 9.5 GHz with this nonuniformity taken into account in Fig. 14(b), where the result with a uniform bias magnetic field is also given for reference. It turns out that there is only a slight shift of the transmission spectrum if the bias magnetic field is nonuniform, but all the physics discussed in this work remains the same.

-
- [1] C. M. Bender and S. Boettcher, *Phys. Rev. Lett.* **80**, 5243 (1998).
 [2] I. Rotter, *J. Phys. A* **42**, 153001 (2009).
 [3] N. Moiseyev, *Non-Hermitian Quantum Mechanics* (Cambridge University Press, Cambridge, 2011).
 [4] W. D. Heiss, *J. Phys. A* **45**, 444016 (2012).
 [5] C. E. Rüter, K. G. Makris, R. El-Ganainy, D. N. Christodoulides, M. Segev, and D. Kip, *Nat. Phys.* **6**, 192 (2010).
 [6] A. Guo, G. J. Salamo, D. Duchesne, R. Morandotti, M. Volatier-Ravat, V. Aimez, G. A. Siviloglou, and D. N. Christodoulides, *Phys. Rev. Lett.* **103**, 093902 (2009).
 [7] A. Regensburger, C. Bersch, M. Miri, G. Onishchukov, D. N. Christodoulides, and U. Peschel, *Nature (London)* **488**, 167 (2012).
 [8] K. G. Makris, R. El-Ganainy, D. N. Christodoulides, and Z. H. Musslimani, *Phys. Rev. Lett.* **100**, 103904 (2008).
 [9] B. Peng, S. K. Özdemir, S. Rotter, H. Yilmaz, M. Liertzer, F. Monifi, C. M. Bender, F. Nori, and L. Yang, *Science* **346**, 328 (2014).
 [10] L. Feng, Z. J. Wong, R.-M. Ma, Y. Wang, and X. Zhang, *Science* **346**, 972 (2014).
 [11] H. Hodaei, M. Miri, M. Heinrich, D. N. Christodoulides, and M. Khajavikhan, *Science* **346**, 975 (2014).
 [12] M. Brandstetter, M. Liertzer, C. Deutsch, P. Klang, J. Schöberl, H. E. Türeci, G. Strasser, K. Unterrainer, and S. Rotter, *Nat. Commun.* **5**, 4034 (2014).
 [13] Y. D. Chong, L. Ge, and A. D. Stone, *Phys. Rev. Lett.* **106**, 093902 (2011).
 [14] L. Ge, Y. D. Chong, S. Rotter, H. E. Türeci, and A. D. Stone, *Phys. Rev. A* **84**, 023820 (2011).
 [15] J. Doppler, A. A. Mailybaev, J. Böhm, U. Kuhl, A. Girschik, F. Libisch, T. J. Milburn, P. Rabl, N. Moiseyev, and S. Rotter, *Nature (London)* **537**, 76 (2016).
 [16] S. Longhi, *Phys. Rev. Lett.* **103**, 123601 (2009).
 [17] R. Fleury, D. L. Sounas, and A. Alù, *Phys. Rev. Lett.* **113**, 023903 (2014).
 [18] J. Wiersig, *Phys. Rev. Lett.* **112**, 203901 (2014).
 [19] Y. Sun, W. Tan, H. Q. Li, J. Li, and H. Chen, *Phys. Rev. Lett.* **112**, 143903 (2014).
 [20] L. Chang, X. Jiang, S. Hua, C. Yang, J. Wen, L. Jiang, G. Li, G. Wang, and M. Xiao, *Nat. Photon.* **8**, 524 (2014).
 [21] K. Ding, G. Ma, M. Xiao, Z. Q. Zhang, and C. T. Chan, *Phys. Rev. X* **6**, 021007 (2016).
 [22] B. Dietz, H. L. Harney, O. N. Kirillov, M. Miski-Oglu, A. Richter, and F. Schäfer, *Phys. Rev. Lett.* **106**, 150403 (2011).
 [23] B. Zhen, C. W. Hsu, Y. Igarashi, L. Lu, I. Kaminer, A. Pick, S. L. Chua, J. D. Joannopoulos, and M. Soljačić, *Nature (London)* **525**, 354 (2015).
 [24] N. X. A. Rivolta and B. Maes, *Opt. Lett.* **40**, 3922 (2015).
 [25] H. Benisty, A. Lupu, and A. Degiron, *Phys. Rev. A* **91**, 053825 (2015).
 [26] Y. Lumer, Y. Plotnik, M. C. Rechtsman, and M. Segev, *Phys. Rev. Lett.* **111**, 263901 (2013).
 [27] A. U. Hassan, H. Hodaei, M. A. Miri, M. Khajavikhan, and D. N. Christodoulides, *Phys. Rev. A* **92**, 063807 (2015).
 [28] D. M. Pozar, *Microwave Engineering* (Wiley, New York, 2005).
 [29] www.comsol.com
 [30] A. B. Yakovlev and G. W. Hanson, *IEEE Trans. Microwave Theory Tech.* **51**, 583 (2003).
 [31] Y. Poo, R. X. Wu, Z. Lin, Y. Yang, and C. T. Chan, *Phys. Rev. Lett.* **106**, 093903 (2011).
 [32] H. Xu, D. Mason, L. Jiang, and J. G. E. Harris, *Nature (London)* **537**, 80 (2016).
 [33] T. J. Milburn, J. Doppler, C. A. Holmes, S. Portolan, S. Rotter, and P. Rabl, *Phys. Rev. A* **92**, 052124 (2015).